

# HVAQ: A High-Resolution Vision-Based Air Quality Dataset

Zuohui Chen\*, Tony Zhang\*, Zhuangzhi Chen, Yun Xiang<sup>†</sup>, Qi Xuan, Robert P. Dick

**Abstract**—Air pollutants, such as particulate matter, strongly impact human health. Most existing pollution monitoring techniques use stationary sensors, which are typically sparsely deployed. However, real-world pollution distributions vary rapidly in space and the visual effects of air pollutant can be used to estimate concentration, potentially at high spatial resolution. Accurate pollution monitoring requires either densely deployed conventional point sensors, at-a-distance vision-based pollution monitoring, or a combination of both.

This paper makes the following contributions: (1) we present a high temporal and spatial resolution air quality dataset consisting of PM2.5, PM10, temperature, and humidity data; (2) we simultaneously take images covering the locations of the particle counters; and (3) we evaluate several vision-based state-of-art PM concentration prediction algorithms on our dataset and demonstrate that prediction accuracy increases with sensor density and image. It is our intent and belief that this dataset can enable advances by other research teams working on air quality estimation.

**Index Terms**—Air pollution, particulate matter, high-resolution dataset, image analysis, evaluation.

## I. INTRODUCTION

**A**IR pollution is a serious threat to human health. It is closely related to disease and death rates [1]–[5]. The world health organization estimates that 2.4 million people die annually from causes associated with air pollution [6]. The most common air pollutants are particulate matter (PM), sulfur dioxide, and nitrogen dioxide. This work focuses on PM, which can increase the rate of cardiovascular, respiratory, and cerebrovascular diseases [7], [8]. Air monitoring stations are widely used to estimate air pollution concentrations. [9]. However, the limited number of sensors and therefore, low spatial density makes them inaccurate (see Figure 1).

Low measurement spatial density makes it inaccurate for the area far away from air monitoring stations. PM has heterogeneous sources [10], e.g., automobiles exhausting, dust, cooking, manufacturing, and building construction etc. The PM concentrations are correlated with source distributions. For example, numerous factors, including wind, humidity, and geography [11], [12], are related to PM distributions. Therefore, air pollution concentration varies within a relatively short distance: relying on existing sparse, stationary monitoring

Z. Chen, Z. Chen, Y. Xiang (<sup>†</sup>corresponding author, email: xiangyun@zjut.edu.cn), and Q. Xuan are with the Institute of Cyberspace Security, Zhejiang University of Technology, Hangzhou 310023, China. R. Dick and T. Zhang are with the EECS Department, University of Michigan, Ann Arbor, U.S.A.

Authors with \* contributed equally to this work.

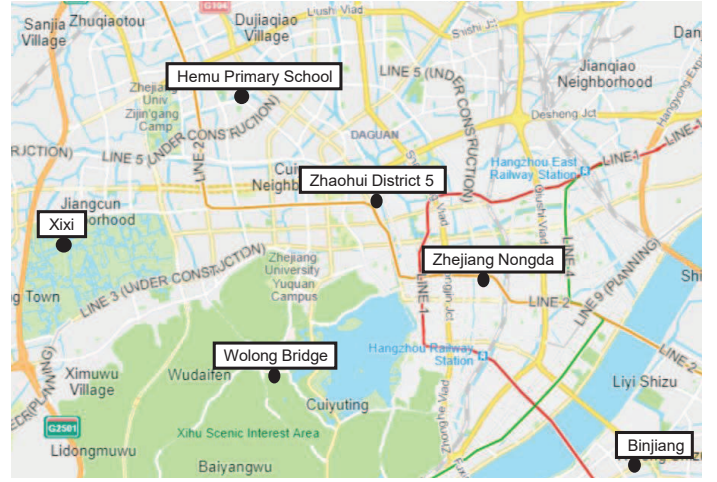


Fig. 1. The distribution of air monitoring stations in Hangzhou. On average, there is one monitoring site for every 35 square kilometers.

stations can lead to inaccurate estimation of the high-resolution pollution field.

Increasing sensor density or adding image sensors supporting high spatial resolution captures can increase estimation accuracy and resolution. Air quality can be estimated by analyzing the visual haze effect caused by particles and gasses [13]. The image data may be derived from several sources such as social media [14] and digital cameras [15]. The ground truth data are typically derived from the nearest air quality station and have low spatial resolution. Existing approaches are generally inaccurate except near the sparsely deployed sensing stations. Moreover, they generally assume homogeneous distributions of particles and gases within images, implying consistent light attenuation. However, in reality, pollution concentration varies rapidly in space. Thus, accurate evaluation and validation of vision-based estimation algorithms requires high-resolution datasets [16].

In this paper, we present a dataset containing high spatial and temporal resolution pollution measurements and the corresponding images. The sensors are deployed at several locations within the camera field of view. The dataset also contains auxiliary information including GPS locations, humidity, and temperature. This paper makes the following contributions.

- 1) It contains temporally and spatially dense PM data for the evaluation and validation of pollution concentration estimation algorithms.
- 2) In addition to PM data, it also contains images covering the distributed particle counter sensors, enabling use

in training and evaluation of vision-based air pollution estimation or real-time forecasting techniques. Vision-based algorithms have the potential for high spatial and temporal resolution and this is the first dataset supporting both vision and sensor readings.

3) We evaluate several vision-based state-of-art PM concentration predication algorithms on our dataset and demonstrate that prediction accuracy increases with sensor density and the use of images.

The rest of the paper is organized as follows. Section II summarizes related work. Section III and Section IV describe our data collection and analysis process. Section V describes the experimental results. Section VI concludes the paper.

## II. RELATED WORK

The related work can be generalized into three categories: environment monitoring methods, pollutant estimation techniques, and vision-based techniques.

### A. Environment Monitoring Methods

Most existing air quality monitoring systems [17] have low temporal and spatial resolution. For example, Janssens-Maenhout et al. [18] provide a harmonized gridded air pollution emission dataset. This dataset includes multiple pollutants on a global scale with  $0.1^\circ \times 0.1^\circ$  spatial resolution (latitude and longitude). It has global coverage but low resolution. Our dataset is limited to one city but is high resolution. De et al. [19] provide an air quality dataset containing 9,358 instances of hourly averaged responses from metal oxide chemical sensors. Devices are deployed in a highly polluted area in Italy at high spatial resolution. However, they do not include corresponding images. Li et al. [20] provide a dataset for mobile air quality measurements in Zurich. They use sensor boxes installed on top of mobile trams. Static installations are also deployed close to high-quality reference stations for calibration. Their sensors move around the city, recording every 5 s, and therefore are high spatial and temporal resolution. Our dataset is also high-resolution but, in contrast, contains corresponding images.

### B. Pollutant Estimation Techniques

Chakma et al. [21] describe an air quality analysis method using hourly PM2.5 data provided by the U.S. embassy in Beijing. They quantify pollution into 3 levels, thus formulating the estimation problem as a classification problem. In contrast, our approach estimates non-quantized concentrations. Zhang et al. [22] use surveillance cameras to construct an outdoor air quality image dataset and extract image features to predict air quality. Our data contains higher quality pictures that cover an area of approximately  $2 \text{ km}^2$  and there are 10 sensors within this area. Brauer et al. [23] study the impact of air pollution on population health and evaluate the trends of relative risk factors based on the dataset gathered by Janssens-Maenhout et al. [18]. Our dataset can also be used, together with epidemiological models, to estimate the impact of pollution on people.

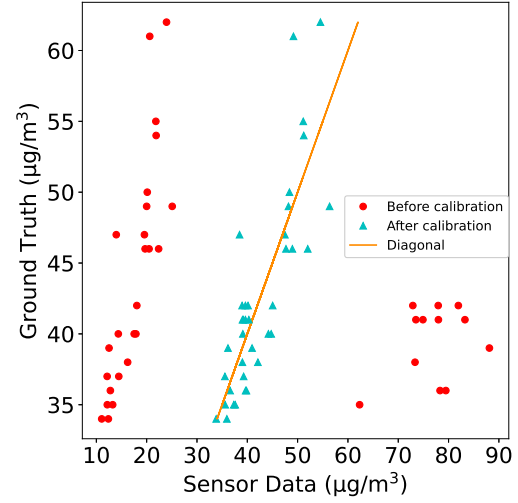


Fig. 2. Uncalibrated and calibrated pollution concentration. The straight line is the fitted calibration line.

### C. Image-based Techniques

Vision-based method is becoming popular not only in industry applications [24], [25], but also in the estimation of PM concentration [26]–[28] due to its convenience and low cost. Li et al. [14] analyze photos acquired from social media and establish the correlation between visual haze and PM2.5 concentration. Gu et al. [29] designed vision-based predictor of PM2.5 concentration. It requires low-pollution reference images for each area of interest. Liu et al. [15] estimate PM2.5 using support vector regression on six features extracted from images. Zhang and Dick [13] estimate multiple pollution concentrations from images using scattering and absorption models. However, it is unclear how these methods work on high-resolution data. Our dataset makes it possible to evaluate them in a high-resolution scenario.

To the best of our knowledge, there is no existing dataset containing both high-resolution data from point measurement devices such as particle counters and the corresponding images.

## III. SENSOR DEPLOYMENT

This section describes our data gathering system and our deployment.

### A. Sensor Calibration

The sensing platform is equipped with humidity and temperature sensors. The precision is 3% relative humidity (RH) and  $\pm 0.3^\circ \text{C}$ . The PM sensor can detect particles with  $0.3 \mu\text{m}$  to  $10 \mu\text{m}$  diameters using laser scattering. Scattered light intensity in a specific direction enables particle size estimation [30].

We calibrated our particle counting sensors to measurements from the air quality monitoring site of Hangzhou Meteorolog-

TABLE I  
GPS Locations of Our Sensors and Picture.

Location	P1	P2	P3
Longitude	120.153173°	120.156252°	120.153894°
Latitude	30.269884°	30.270242°	30.27096°
P4	P5	P6	P7
120.156541°	120.153905°	120.15936°	120.155162°
30.283932°	30.27358°	30.273139°	30.278369°
P8	P9	P10	Photo location
120.161912°	120.164792°	120.15488°	120.153955°
30.276465°	30.279437°	30.268726°	30.267191°

TABLE II  
Pairwise Sensors Distance (unit: meter)

	P1	P2	P3	P4	P5	P6	P7	P8	P9	P10
P1	0	113	168	281	464	697	1012	1150	1730	1625
P2	0	211	190	509	603	1040	1089	1537	1660	
P3		0	245	296	575	844	1000	1450	1457	
P4			0	388	413	871	899	1347	1510	
P5				0	464	548	819	1250	1161	
P6					0	625	486	934	1170	
P7						0	656	918	613	
P8							0	448	953	
P9								0	877	
P10									0	

ical Bureau in Hemu Primary School using co-location [31]. The following linear calibration function is used:

$$y = \begin{cases} 1.61x + 16.01 & \text{for } 0 \leq x \leq 30 \text{ and} \\ 0.13x + 29.48 & \text{for } x > 30, \end{cases} \quad (1)$$

where  $x$  is the original value and  $y$  is the calibrated value. The calibration data were gathered during 2 days and the result is shown in Figure 2. Calibration reduces root mean square error (RMSE) from  $32.74 \mu\text{g m}^{-3}$  to  $3.88 \mu\text{g m}^{-3}$ , while the variance for all the data in different locations is  $9.33 \mu\text{g m}^{-3}$ .

### B. Deployment Details

This dataset should contain both high-resolution ground truth data and wide-view images. Some sensors were placed outdoors and close to living areas. The city center is most crowded: it is here that air quality affects people the most. We deploy our sensors in the urban area of Hangzhou, a city of more than 8 million residents, that is frequently affected by high PM2.5 concentrations [32]. Jin et al. [33] show that in the main urban area of Hangzhou, the sources of PM2.5 are biomass burning/construction dust (41.6%), vehicle exhaust/metallurgical dust (29.3%), unknown source (11.2%), oil combustion (9.8%), and soil (8.0%). As shown in Figure 3, we marked the main pollution sources on the map and the sensors are located on two straight lines from the observation point. The GPS locations and distances between each pair of sensors are listed in Table I and Table II, respectively. The sensors are sampled every second and an image is captured every 20 minutes. To derive a wide-view image covering

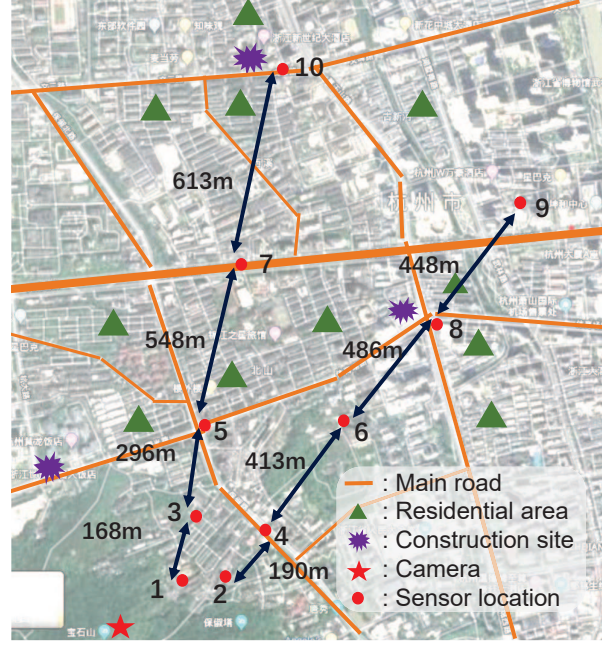


Fig. 3. The distribution of sensors and pollution sources. Sensor locations are numbered in ascending order according to the distance from the camera.

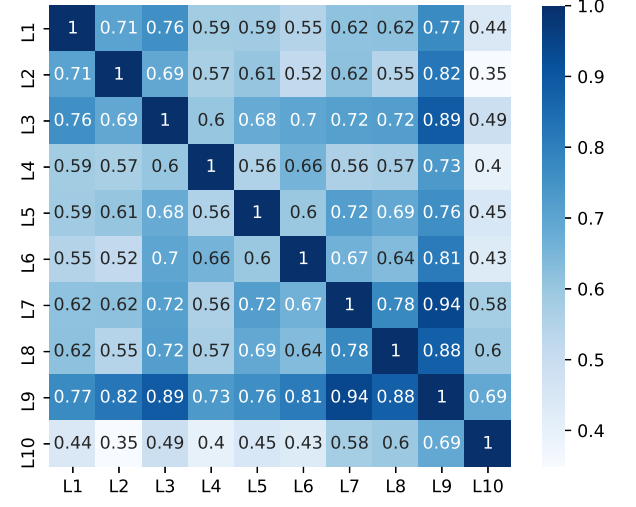


Fig. 4. The confusion matrix for PM2.5 correlation. The number on the axis represents the number of the corresponding location.

all sensor locations, we mount a camera on a quadcopter shown in Figure 6. We use two different approaches to take photos. First, we use a quadcopter equipped with a camera of resolution  $4864 \times 3648$  at 90 m altitude. Moreover, since the quadcopter limits carrying weight and battery capacities, we also take pictures at a fixed location on the mountain top with a resolution of  $2592 \times 1936$ . The parameters of our cameras are listed in Table III.

A camera (about \$30) is much less expensive than the total cost of 10 sensor and other materials in the deployment (about \$670). Predicting air pollution concentrations from images is

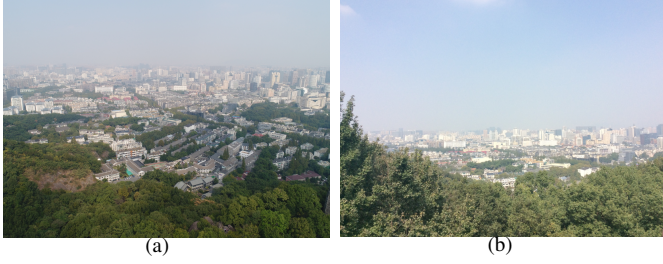


Fig. 5. (a) High altitude quadcopter view and (b) low altitude camera view.



Fig. 6. The quadcopter (Dji Phantom 4) used in our deployment.

TABLE III  
Quadcopter Camera Parameter.

Pixel	Sensor	FOV	Lens
20000000	1 inch CMOS	84°	8.8 mm/24 mm

a more convenient and less expensive approach than directly collecting air quality data from sensors.

#### IV. DATASET ANALYSIS

This section describes our analysis process and various concentration prediction techniques. Specifically, we aim to answer the following questions through experimentation and data analysis.

- Q1** What is the impact of environmental conditions on measurement accuracy?
- Q2** What are the spatial variation characteristics of PM2.5 concentration?
- Q3** How does pollution concentration correlation change as a function of distance?
- Q4** How much do vision-based techniques increase estimation accuracy?

##### A. Environmental Factors Correlations

Environmental factors like weather conditions affect sensor readings. For the deployments on Oct. 19 and Nov. 10, we

TABLE IV  
PM2.5 Correlation with PM10 and Environmental Factors on Oct. 19 and Nov. 10

	PM2.5	Temperature	Humidity
PM2.5	1.0	0.298	0.306
Temperature	0.298	1.0	0.808
Humidity	0.306	0.808	1.0

TABLE V  
Statistics for PM and Environmental Data

Data in Different Days	Standard Deviation	Data Range	Average Value	Date
PM2.5 ( $\mu\text{g m}^{-3}$ )	2.03	4.56	13.93	Jul. 24
PM2.5 ( $\mu\text{g m}^{-3}$ )	2.22	5.11	25.03	Jul. 06
PM2.5 ( $\mu\text{g m}^{-3}$ )	6.68	22.21	56.90	
Temperature (°C)	5.64	16.02	26.40	Oct. 19
RH (%)	12.36	37.63	45.13	
PM2.5 ( $\mu\text{g m}^{-3}$ )	4.77	16.51	48.76	
Temperature (°C)	4.53	14.21	24.79	Nov. 10
RH (%)	10.20	34.71	40.16	

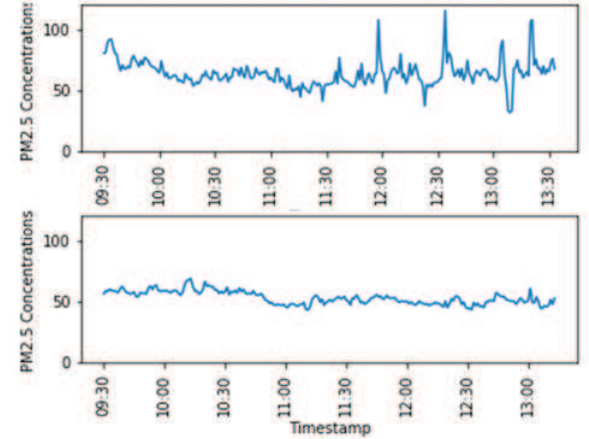


Fig. 7. The concentrations of 2 different locations in our Oct. 19 deployment.

calculate the  $R^2$  correlation coefficients for PM2.5 and several environmental factors as follows:

$$R^2 = 1 - \frac{\sum(y_i - \hat{y}_i)^2}{\sum(y_i - \bar{y}_i)^2}, \quad (2)$$

where  $y_i$  is the sensor reading,  $\hat{y}_i$  is the reading of a correlated sensor, and  $\bar{y}_i$  is the mean of all the remaining sensors.

**A1 Environmental conditions have limited impact.** The results in Table IV shows that the correlations between PM2.5 and weather factors are low but the correlation between PM2.5 and PM10 is high. We therefore do not include temperature and humidity in our calibration functions.

##### B. Correlations of PM Readings

Our measurements show that it takes at least 10 minutes for concentration to change by  $10 \mu\text{g m}^{-3}$ . The data sampling period is one minute; adequate given the slow rate of change.

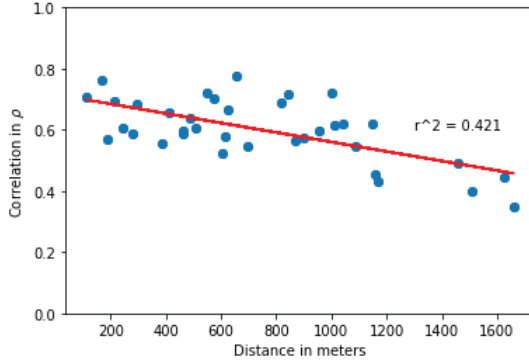


Fig. 8. Pairwise correlation between sensors for Oct. 19 and Nov. 10 corresponding to their distance.

We measure the spatial variation of pollution by calculating the standard deviations of all the sensors.

$$\sigma = \sqrt{\frac{\sum_{i=1}^k (x_i - \bar{x})^2}{k}}, \quad (3)$$

where  $\bar{x}$  is the mean of all data in one day,  $k$  is the amount of data.

**A2 Spatial variation of PM2.5 is high.** As shown in Table V and Figure 7, the 2 locations have different concentrations and variation trends. Moreover, the large data range suggests that multiple pollution levels coexist in a single image.

**A3 The spatial pollutant distribution is correlated based on the distance.** The local PM readings are correlated. We quantify the correlations for further analysis. Figure 8 shows the sensors correlation as a function of pairwise distances. The correlation is measured by Spearman correlation coefficient  $\rho$  that follows

$$\rho = 1 - \frac{6 \sum d_i^2}{N(N^2 - 1)}, \quad (4)$$

where  $d_i$  represents the position difference of the paired variables after the two variables are sorted separately,  $N$  is the total number of samples. The slope of the fitting line is  $0.155 \text{ km}^{-1}$  and the coefficient of determination ( $R^2$ ) is 0.421, which implies that closer sensors have the potential to improve estimation accuracy.

Figure 4 shows the sensor correlations during the Nov. 10 and Oct. 19 deployments. We expect the correlations to decrease with increasing inter-sensor distances. The deployment results confirm our hypothesis. However, the nearest air monitoring sites in Hangzhou are 4.4 km from each other. Sparsely distributed air monitoring stations can not accurately cover a large area. A sensor network combined with vision-based analysis can improve the estimation results significantly, as shown in Section V.

## V. EXPERIMENTAL RESULTS

In this section, we evaluate the implications of changing sensor density and using vision-based techniques on estimation accuracy. Specifically, we estimate PM2.5 concentration based on vision-based analysis using the transmission information

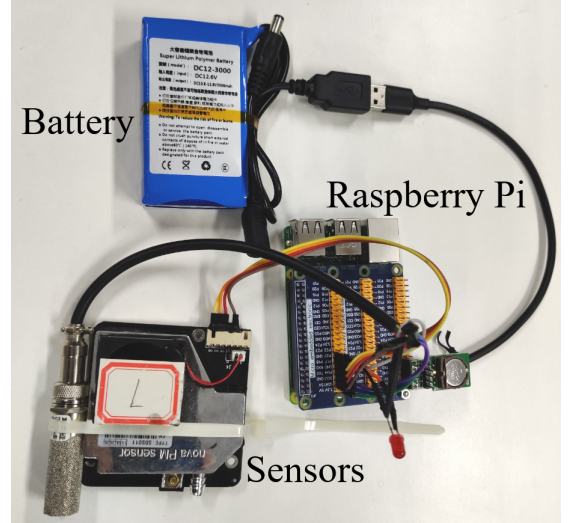


Fig. 9. The sensing platform consisting of battery, Raspberry Pi, and sensors.

and standard deviation, then compare the performance of several state-of-art algorithms.

### A. Experimental Setup

We designed a portable sensing platform to collect, process, and transmit data, as shown in Figure 9. The system battery life is 3.5 hours.

We use the following algorithms to estimate pollutant concentration from the measured data.

- 1) **Random forest regression (RFR):** This is a widely used algorithm for regression and classification. It combines multiple weak models to form a strong model with much better performance. Random forests contain multiple, unrelated decision trees. The final output depends on the decisions of all trees.
- 2) **Gradient boosting regression (GBR):** This method combines a group of weak learners with low complexity and low training cost. It reduces the problem of overfitting and modifies the weights at each training round to produce a strong learner. Gradient boosting modifies its models based on the gradient descent direction of the loss functions of the previously established models.
- 3) **Support vector regression (SVR):** Support vector regression aims to find a regression plane with minimal distance to the dataset. Generally, there is a kernel function mapping data to high-dimensional space for better performance. In this work, we use the RBF kernel function in SVR, set the regularization parameter “c” to 200, and use default values for all other parameters.

We use the following equation to combine sensor readings and image properties:

$$S(x, t) = G(s_1(t), s_2(t), \dots, s_n(t), \tilde{t}(x, t), \theta(t)), \quad (5)$$

where  $x$  is the location index,  $S(x, t)$  is the concentration estimation at time  $t$ ,  $s_1, s_2, \dots, s_n$  are the available  $n$  sensors,  $\tilde{t}(x, t)$  is the transmission information at time  $t$ ,  $\theta(t)$  is the

standard deviation of gray-scale image, and  $G$  is the estimation algorithm, which refers to RFR, GBR, or SVR.

We use data from Jul. 24, Oct. 19, and Nov. 10 for all timestamps and use the mean absolute error (MAE) as the evaluation criteria. There are two kinds of images in different batches of our data, the first case is ground level on the mountain (78 m), the second case is using a quadcopter on the mountain (78 m+90 m). We divide our data into low-batch and high-batch dataset according to the image types, evaluate these algorithms separately on different images. Each dataset is divided as follows: 75% of the data and images are randomly selected as a training set and the rest are the testing set. We run the prediction model 50 times per random split of the training and testing datasets.

### B. Image Enhanced Concentration Estimation

Images can provide global information on the environment and be used to estimate PM concentrations in large areas. The atmospheric model describing an image influenced by haze follows [34]:

$$\mathbf{I}(x) = \mathbf{J}(x)t(x) + \mathbf{A}(1 - t(x)), \quad (6)$$

where  $x$  is the pixel location,  $\mathbf{I}$  is the observed image,  $\mathbf{J}$  is the scene radiance (image without any haze),  $\mathbf{A}$  is the atmospheric light,  $t$  is the transmission function.

Images with higher air pollution tend to look hazier due to lower transmission and contrast. Hence, image features that account for the level of haze provide useful information for pollutant concentration estimation. The dark channel prior, which has been widely used for haze removal, can be used to estimate the transmission of each image pixel. The dark channel prior method is based on the observation that in most haze-free patches, at least one color channel has some pixels with very low intensities. The dark channel is defined as the minimum of all pixel colors in a local patch and can be calculated using the following equation [35]:

$$J_{dark}(x) = \min_{c \in r, g, b} \left( \min_{y \in \Omega_r(x)} J^c(y) \right), \quad (7)$$

where  $J^c$  is an RGB channel of  $\mathbf{J}$  and  $\Omega_r(x)$  is a local patch centered at  $x$  with the size of  $15 \times 15$ . Assume the atmospheric light  $\mathbf{A}$  is given and the transmission in a local patch  $\Omega_r(x)$  is constant, taking the min operation in the local patch on Equation 6, we have

$$\min_{y \in \Omega_r(x)} (I^c(y)) = \tilde{t}(x) \min_{y \in \Omega_r(x)} (J^c(y)) + (1 - \tilde{t}(x))A^c, \quad (8)$$

where  $\tilde{t}(x)$  is the patch's transmission. The min operation is performed on three color channels independently, it is equivalent to

$$\min_{y \in \Omega_r(x)} \left( \frac{I^c(y)}{A^c} \right) = \tilde{t}(x) \min_{y \in \Omega_r(x)} \left( \frac{J^c(y)}{A^c} \right) + (1 - \tilde{t}(x)). \quad (9)$$

By taking the min operation among three color channels,

we have

$$\begin{aligned} \min_c \left( \min_{y \in \Omega_r(x)} \left( \frac{I^c(y)}{A^c} \right) \right) &= \tilde{t}(x) \min_c \left( \min_{y \in \Omega_r(x)} \left( \frac{J^c(y)}{A^c} \right) \right) \\ &\quad + (1 - \tilde{t}(x)). \end{aligned} \quad (10)$$

According to the definition of dark channel prior, the dark channel  $J_{dark}$  of the haze-free radiance  $\mathbf{J}$  tends to be zero

$$J_{dark}(x) = \min_c \left( \min_{y \in \Omega_r(x)} J^c(y) \right) = 0. \quad (11)$$

Because  $A^c$  is always positive, this lead to

$$\min_c \left( \min_{y \in \Omega_r(x)} \frac{J^c(y)}{A^c} \right) = 0. \quad (12)$$

Substituting Equation 12 into Equation 10, we can estimate the transmission as follows.

$$\tilde{t}(x) = 1 - \min_c \left( \min_{y \in \Omega_r(x)} \frac{I^c(y)}{A^c} \right). \quad (13)$$

In practice, the atmosphere always contains some haze, which provides depth information. We can optionally keep a small amount of haze by introducing a constant parameter  $\omega$  ( $0 < \omega < 1$ ) into Equation 13

$$\tilde{t}(x) = 1 - \omega \min_c \left( \min_{y \in \Omega_r(x)} \frac{I^c(y)}{A^c} \right). \quad (14)$$

We fix the value of  $\omega$  to 0.95 because it is application-based. The atmospheric light  $A$  is estimated through this procedure: we pick the top 0.1% brightest pixels in the dark channel and the input image  $\mathbf{I}$  to calculate the atmospheric light. For each hazy image in our dataset, we take the average of the pixel-level transmissions estimated using Equation 14. The resulting average is used for low-batch data.

We convert the RGB image to a gray-scale image, then calculate the standard deviation of all the pixels. Because the standard deviation is closely related to haze density [36]. The scattering coefficient is the degree of haze density. The higher the scattering coefficient, the higher the haze density. The transmission function is

$$t(x) = e^{\beta d(x)}, \quad (15)$$

where  $\beta$  is the scattering coefficient, and  $d$  is the depth. Substituting Equation 15 into Equation 6, we have

$$\mathbf{I}_g(x) = \mathbf{J}(x)e^{\beta d(x)} + \mathbf{A}(1 - e^{\beta d(x)}). \quad (16)$$

The variance of a gray-scale image is

$$\begin{aligned} \sigma_{I_g}^2 &= \frac{1}{N} \sum_{i=1}^N (I_g(i) - \frac{1}{N} \sum_{j=1}^N I_g(j))^2 \\ &= e^{2\beta d(x)} \frac{1}{N} \sum_{i=1}^N (J(i) - \frac{1}{N} \sum_{j=1}^N J(j))^2, \end{aligned} \quad (17)$$

where  $I_g$  is the gray-scale image and  $N$  is the number of pixels in the image. When  $\beta = 0$ , we have

$$\sigma_0^2 = \frac{1}{N} \sum_{i=1}^N (J(i) - \frac{1}{N} \sum_{j=1}^N J(j))^2. \quad (18)$$

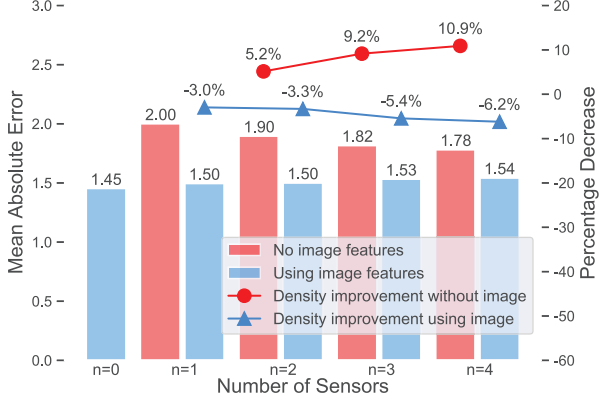


Fig. 10. Sensor density improvement for GBR on high-batch data.

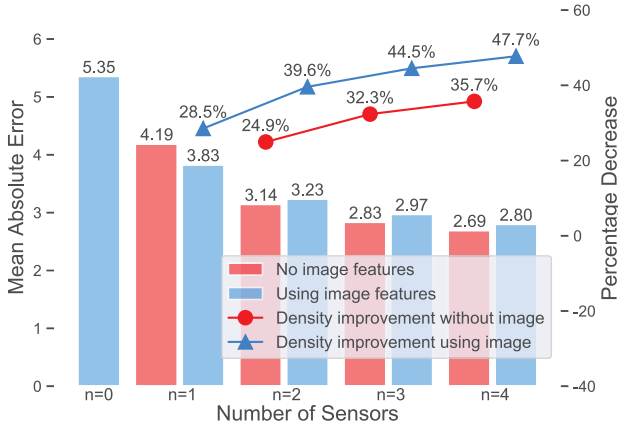


Fig. 11. Sensor density improvement for GBR on low-batch data.

Combining Equation 18 and Equation 17 yields

$$\sigma_{I_g} = e^{-2\beta} \sigma_0^2. \quad (19)$$

After taking the logarithm of both sides, the scattering coefficient can be expressed as

$$\beta = \ln \sigma_0 - \ln \sigma_{I_g}. \quad (20)$$

When  $\beta = 0$ , the variance of the scene radiance approximates 1. Thus we have

$$\beta = 1 - \ln \sigma_{I_g}. \quad (21)$$

Therefore we can estimate the concentration using the standard deviation of the gray-scale image. The standard deviation is used for high-batch data.

### C. Concentration Estimation Results

For each available sensor deployment location, we speculatively remove one or more sensor's data and use estimation techniques with access to the remaining sensors to infer concentration(s), thereby allowing comparison with ground truth measurements. We investigate the impact of the number of sensors on the estimation accuracy by using all possible combinations of speculatively removed sensors and averaging the results. We also consider the impact of using image data on estimation accuracy.



Fig. 12. Image improvement for GBR on high-batch data.

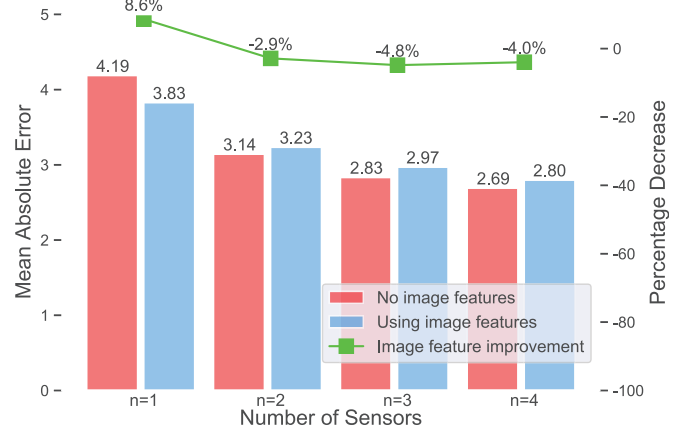


Fig. 13. Image improvement for GBR on low-batch data.

We select the best-performing algorithm GBR to show our experiment result. The density improvements in Figure 10 and Figure 11 are compared with the  $n = 0$  case when images are not used. If image features are used, the improvements are compared with the  $n = 1$  case. As sensor density increases, the MAE of the estimation result significantly drops. This implies that a high-resolution PM sensor network can improve estimation accuracy. Moreover, as shown in Figure 8, sensor correlations drop when distance increases. This is the reason for the estimation accuracy improves with increasing sensor density. In the case of using 4 nearest sensors, sensor density can improve estimation accuracy by 23.3% on average without using images, and 20.75% when using images.

**A4 The estimation accuracy can be improved significantly when enhanced by vision-based techniques.** As shown in Figure 12 and Figure 13, PM2.5 concentration prediction accuracy improves when images are used. In the case of  $n = 0$ , we average all the available concentrations. MAE is  $20.821 \mu\text{g m}^{-3}$  for high-batch data and  $6.929 \mu\text{g m}^{-3}$  for low-batch data. When images are used, MAE drops to  $1.45 \mu\text{g m}^{-3}$  and  $5.35 \mu\text{g m}^{-3}$  respectively. For the case where  $n = 1$ , when we use the PM2.5 concentrations of the nearest available sensor for estimation image data improves prediction accuracy by 16.9% on average. The benefits of using images are greatest when the fewest particle counters are used.

TABLE VI  
P-Values of GBR, SVR, and RFR on High-Batch Data

GBR			
n=1	n=2	n=3	n=4
< 0.001	< 0.001	< 0.001	0.103
SVR			
n=1	n=2	n=3	n=4
< 0.001	< 0.001	< 0.001	0.002
RFR			
n=1	n=2	n=3	n=4
0.005	0.074	0.440	0.767

TABLE VII  
P-Values of GBR, SVR, and RFR on Low-Batch

GBR			
n=1	n=2	n=3	n=4
< 0.001	0.034	< 0.001	< 0.001
SVR			
n=1	n=2	n=3	n=4
0.106	0.012	< 0.001	< 0.001
RFR			
n=1	n=2	n=3	n=4
0.009	0.069	0.001	0.002

We use the two-sided t-test to determine whether the improvement is systemic, or the result of noise. The t-test applies to normal random processes, which are validated by the Shapiro-Wilks test that both results of using images or not follow normal distributions. We hypothesize that there is no effective difference between the mean of MAE distribution using images and the mean of MAE distribution of not using images, i.e., that any measured difference is due only to chance. If the p-value is below 0.05, we can reject the hypothesis and state that there is a difference between the results of whether using images.

As shown in Table VII and Table VII, on low-batch data, the p-values of GBR in all cases are less than 0.05, and on high-batch data, GBR's p-values are less than 0.05 only when  $n \leq 3$ . This implies that when  $n \leq 3$ , we are confident that using images improves the estimation.

Certain fixed-location images show slightly negative results for the GBR method. Since the fixed-location images are taken from a low altitude, some of the sensors locations are blocked by buildings. For the quadcopter images taken at a higher altitude, all estimation techniques improve accuracy. In general, images decrease MAE by 8.44% on average, when  $n \leq 1$ , adding a camera to collect images helps more than adding more sensors.

Increasing sensor density and using images changes the relative accuracies of the estimation algorithms. When we use only one sensor and no images, RFR has lower MAE than GBR on low-batch data. When the sensor density is increased ( $n = 4$ ) and images used, GBR outperforms RFR. This result demonstrates that it is important to evaluate estimation algorithms using appropriate sensor densities and access to image

data. A sparsely deployed and less accurate sensor network can lead to false conclusions about pollution concentrations, and about which pollution concentration estimation algorithms are most accurate.

To summarize, higher sensor densities and image data both improve estimation accuracy, and adding image data has a similar effect to increasing particle counter density by 0.61 sensors  $\text{km}^{-2}$ . Of the three estimation techniques evaluated, GBR had the highest accuracy with  $\text{MAE} = 1.45 \mu\text{g m}^{-3}$  in all the data.

## VI. CONCLUSION

This paper has presented a PM dataset with a high temporal and spatial resolutions. In contrast with existing datasets, it also contains images covering the locations of stationary point sensors, making it suitable for evaluating and validating vision-based pollution estimation algorithms. Through our analysis, we find that (1) environmental conditions have limited impact on PM concentration; (2) spatial variation of PM2.5 is high; (3) the spatial pollutant distribution is correlated based on the distance; and (4) the estimation accuracy can be improved significantly using vision-based techniques. We also evaluate our data using state-of-art prediction methods. Accuracy correlates with density with a coefficient of  $0.2875 \mu\text{g m}^{-3}$  MAE per sensor and that vision-based estimation improves accuracy by  $0.1813 \mu\text{g m}^{-3}$  MAE, on average.

## ACKNOWLEDGMENT

This work was supported in part by NSF under award CNS-2008151 and in part by the National Natural Science Foundation of China (61572439) and Zhejiang Provincial Natural Science Foundation of China (LY18F030021, LR19F030001). The authors would like to thank Zhuangzhuang Liu, Qing Yuan, Qiang Zheng, Wencheng Liu, Chengchao Zhu, Lijie Sun, Xinhui Zhang, Xujie Song, and Jiakang Zhao, who helped with the sensor deployments.

## REFERENCES

- [1] K. Naddafi, M. S. Hassanvand, M. Yunesian, F. Momeniha, R. Nabizadeh, S. Faridi, and A. Gholampour, "Health impact assessment of air pollution in megacity of Tehran, Iran," *Iranian J. of Environmental Health Science & Engineering*, vol. 9, no. 1, p. 28, 2012.
- [2] H. Nourmoradi, Y. O. Khanabadi, G. Goudarzi, S. M. Daryanoosh, M. Khoshgoftar, F. Omidi, and H. Armin, "Air quality and health risks associated with exposure to particulate matter: a cross-sectional study in Khorramabad, Iran," *Health Scope*, vol. 5, no. 2, 2016.
- [3] S. Poduri, A. Nimkar, and G. S. Sukhatme, "Visibility monitoring using mobile phones," *Annual Report: Center for Embedded Networked Sensing*, pp. 125–127, 2010.
- [4] B. Chen and H. Kan, "Air pollution and population health: a global challenge," *Environmental Health and Preventive Medicine*, vol. 13, no. 2, pp. 94–101, 2008.
- [5] F. J. Kelly and J. C. Fussell, "Air pollution and public health: emerging hazards and improved understanding of risk," *Environmental Geochemistry and Health*, vol. 37, no. 4, pp. 631–649, 2015.
- [6] I. Abubakar, T. Tillmann, and A. Banerjee, "Global, regional, and national age-sex specific all-cause and cause-specific mortality for 240 causes of death, 1990–2013: a systematic analysis for the Global Burden of Disease Study 2013," *Lancet*, vol. 385, no. 9963, pp. 117–171, 2015.
- [7] S. Feng, D. Gao, F. Liao, F. Zhou, and X. Wang, "The health effects of ambient PM2. 5 and potential mechanisms," *Ecotoxicology and Environmental Safety*, vol. 128, pp. 67–74, 2016.

[8] J. O. Anderson, J. G. Thundiyil, and A. Stolbach, "Clearing the air: a review of the effects of particulate matter air pollution on human health," *J. of Medical Toxicology*, vol. 8, no. 2, pp. 166–175, 2012.

[9] R. A. Rohde and R. A. Muller, "Air pollution in China: mapping of concentrations and sources," *PLoS one*, vol. 10, no. 8, 2015.

[10] Y. Zhang, J. Cai, S. Wang, K. He, and M. Zheng, "Review of receptor-based source apportionment research of fine particulate matter and its challenges in China," *Science of the Total Environment*, vol. 586, pp. 917–929, 2017.

[11] G. Lin, J. Fu, D. Jiang, W. Hu, D. Dong, Y. Huang, and M. Zhao, "Spatio-temporal variation of PM2.5 concentrations and their relationship with geographic and socioeconomic factors in China," *Int. J. of Environmental Research and Public Health*, vol. 11, no. 1, pp. 173–186, 2014.

[12] X. Zhao, W. Zhou, L. Han, and D. Locke, "Spatiotemporal variation in PM2.5 concentrations and their relationship with socioeconomic factors in China's major cities," *Environment Int.*, vol. 133, p. 105145, 2019.

[13] T. Zhang and R. P. Dick, "Estimation of multiple atmospheric pollutants through image analysis," in *Proc. Int. Conf. on Image Processing*, pp. 2060–2064, 2019.

[14] Y. Li, J. Huang, and J. Luo, "Using user generated online photos to estimate and monitor air pollution in major cities," in *Proc. Int. Conf. on Internet Multimedia Computing and Service*, pp. 1–5, 2015.

[15] C. Liu, F. Tsow, Y. Zou, and N. Tao, "Particle pollution estimation based on image analysis," *PLoS one*, vol. 11, no. 2, p. e0145955, 2016.

[16] J. S. Apte, K. P. Messier, S. Gani, M. Brauer, T. W. Kirchstetter, M. M. Lunden, J. D. Marshall, C. J. Portier, R. C. Vermeulen, and S. P. Hamburg, "High-resolution air pollution mapping with Google street view cars: exploiting big data," *Environmental Science & Technology*, vol. 51, no. 12, pp. 6999–7008, 2017.

[17] C. Wen, S. Liu, X. Yao, L. Peng, X. Li, Y. Hu, and T. Chi, "A novel spatiotemporal convolutional long short-term neural network for air pollution prediction," *Science of the Total Environment*, vol. 654, pp. 1091–1099, 2019.

[18] G. Janssens-Maenhout, F. Dentener, J. Van Aardenne, S. Monni, V. Pagliari, L. Orlandini, Z. Klimont, J.-i. Kurokawa, H. Akimoto, T. Ohara *et al.*, "EDGAR-HTAP: a harmonized gridded air pollution emission dataset based on national inventories," *European Commission Publications Office, Ispra (Italy). JRC68434, EUR report*, vol. 25, pp. 299–2012, 2012.

[19] S. De Vito, E. Massera, M. Piga, L. Martinotto, and G. Di Francia, "On field calibration of an electronic nose for benzene estimation in an urban pollution monitoring scenario," *Sensors and Actuators B: Chemical*, vol. 129, no. 2, pp. 750–757, 2008.

[20] J. J. Li, B. Faltings, O. Saukh, D. Hasenfratz, and J. Beutel, "Sensing the air we breathe: the OpenSense Zurich dataset," in *AAAI Conf. on Artificial Intelligence*, 2012.

[21] A. Chakma, B. Vizena, T. Cao, J. Lin, and J. Zhang, "Image-based air quality analysis using deep convolutional neural network," in *Proc. Int. Conf. on Image Processing*, pp. 3949–3952, 2017.

[22] Z. Zhang, H. Ma, H. Fu, L. Liu, and C. Zhang, "Outdoor air quality level inference via surveillance cameras," *Mobile Information Systems*, vol. 2016, 2016.

[23] M. Brauer, G. Freedman, J. Frostad, A. Van Donkelaar, R. V. Martin, F. Dentener, R. v. Dingenen, K. Estep, H. Amini, J. S. Apte *et al.*, "Ambient air pollution exposure estimation for the global burden of disease 2013," *Environmental Science & Technology*, vol. 50, no. 1, pp. 79–88, 2016.

[24] S. Shirmohammadi and A. Ferrero, "Camera as the instrument: the rising trend of vision based measurement," *IEEE Instrumentation & Measurement Magazine*, vol. 17, DOI 10.1109/MIM.2014.6825388, no. 3, pp. 41–47, 2014.

[25] D. Pan, Z. Jiang, Z. Chen, W. Gui, Y. Xie, and C. Yang, "Temperature measurement and compensation method of blast furnace molten iron based on infrared computer vision," *IEEE Trans. on Instrumentation and Measurement*, vol. 68, no. 10, pp. 3576–3588, 2018.

[26] L. P. Clark, V. Sreekanth, B. Bekbulat, M. Baum, S. Yang, P. Baylon, T. R. Gould, T. V. Larson, E. Y. Seto, C. D. Space *et al.*, "Developing a low-cost passive method for long-term average levels of light-absorbing carbon air pollution in polluted indoor environments," *Sensors*, vol. 20, no. 12, p. 3417, 2020.

[27] G. Yue, K. Gu, and J. Qiao, "Effective and efficient photo-based pm2.5 concentration estimation," *IEEE Trans. on Instrumentation and Measurement*, vol. 68, no. 10, pp. 3962–3971, 2019.

[28] G. Li, J. Wu, Z. Luo, and X. Chen, "Vision-based measurement of dust concentration by image transmission," *IEEE Trans. on Instrumentation and Measurement*, vol. 68, DOI 10.1109/TIM.2018.2883999, no. 10, pp. 3942–3949, 2019.

[29] K. Gu, J. Qiao, and X. Li, "Highly efficient picture-based prediction of PM2.5 concentration," *IEEE Trans. on Industrial Electronics*, vol. 66, no. 4, pp. 3176–3184, 2018.

[30] H. Grimm and D. J. Eatough, "Aerosol measurement: the use of optical light scattering for the determination of particulate size distribution, and particulate mass, including the semi-volatile fraction," *J. of the Air & Waste Management Association*, vol. 59, no. 1, pp. 101–107, 2009.

[31] M. Kamionka, P. Breuil, and C. Pijolat, "Calibration of a multivariate gas sensing device for atmospheric pollution measurement," *Sensors and Actuators B: Chemical*, vol. 118, no. 1–2, pp. 323–327, 2006.

[32] G. Liu, J. Li, D. Wu, and H. Xu, "Chemical composition and source apportionment of the ambient PM2.5 in Hangzhou, China," *Particuology*, vol. 18, pp. 135–143, 2015.

[33] Q. Jin, R. Ren, and L. Gong, "Research on the elemental characterization and source apportionment of PM2.5 in main urban area of Hangzhou," *Chinese J. of Health Laboratory Technology*, vol. 27, no. 22, pp. 3200–3205, 2017.

[34] S. G. Narasimhan and S. K. Nayar, "Vision and the atmosphere," *Int. J. of Computer Vision*, vol. 48, no. 3, pp. 233–254, 2002.

[35] K. He, J. Sun, and X. Tang, "Single image haze removal using dark channel prior," *IEEE Trans. on Pattern Analysis and Machine Intelligence*, vol. 33, no. 12, pp. 2341–2353, 2010.

[36] D. Park, D. K. Han, C. Jeon, and H. Ko, "Fast single image de-hazing using characteristics of RGB channel of foggy image," *IEICE Trans. on Information and Systems*, vol. 96, no. 8, pp. 1793–1799, 2013.